

The nascent solar wind: origin and acceleration

Luca Teriaca¹, Giannina Poletto¹, Marco Romoli², Doug A. Biesecker³

lte@arcetri.astro.it, poletto@arcetri.astro.it, romoli@arcetri.astro.it

doug@sungrazer.nascom.nasa.gov

ABSTRACT

High speed solar wind is known to originate in polar coronal holes which, however, are made up of two components: bright, high density regions known as *plumes*, and dark, weakly emitting low density regions known as *interplumes*. Recent space observations have shown that the width of UV lines is larger in interplume regions while observations of the ratio of the O VI doublet lines at 1032 and 1037 Å, at 1.7 solar radii, suggest higher outflows in interplume regions than in plumes at that altitude. These results favor interplumes regions as sources of the fast solar wind. The present work aims at investigating the outflow speed vs. altitude properties of the O VI and H I ions, at heights below 2 solar radii, both in plumes and interplume regions. To this end, we examined SUMER and UVCS observations of a north polar coronal hole taken on 1996 June 3, over the altitude range between 1 and 2 solar radii and, through a Doppler dimming analysis of our data, we show that interplume areas may be really identified as sources of fast wind streams. The behavior of plumes, on the contrary, can be interpreted in terms of static structures embedded in the interplume ambient. We conclude comparing our results with the predictions of theoretical models of the solar wind and giving an empirical estimate of the heating rate, per particle, for H I and O VI ions, in interplume regions at 1.75 and 2.0 solar radii.

Subject headings: solar physics: observation — coronal holes — solar wind: acceleration — spectroscopy: EUV

¹Osservatorio Astrofisico di Arcetri, Largo Enrico Fermi 5, 50125 Firenze, Italy

²Dipartimento di Astronomia e Scienza dello Spazio, Università di Firenze, Largo Fermi 5, 50125 Firenze, Italy

³NOAA/Space Environment Center, 325 Broadway, Boulder, CO 80305, USA

1. Introduction

Polar coronal holes have long been recognized to be the sources of the high speed solar wind (Krieger, Timothy & Roelof 1973), but not much is known yet, about where, within coronal holes, the solar wind originates. White light, UV and soft X-rays images of polar coronal holes revealed these to be highly structured: denser features – rays and plumes – show up within the low density ambient plasma and preserve their identity out to large distances (see e.g. Koutchmy 1977; Walker et al. 1993; DeForest et al. 1997, 2001). Plumes have also been recognized as the site where fluctuations, interpreted as slow magnetosonic waves, are confined: as waves propagate upwards, they steepen and possibly contribute to local heating (DeForest & Gurman 1998; Ofman et al. 1999). Because plumes, if static, can hardly be maintained (their lifetime is on the order of one day or longer), the question arises of the role of plumes in the fast wind origin and acceleration.

Wang (1994), for instance, modeled the mass flow within a polar plume, including the effect of coronal heating and radiative losses, and compared the plasma outflow speed in plumes with the plasma outflow speed from the ambient corona. In the low corona, up to two solar radii, Wang’s models predict the plume outflow speed to be lower than the ambient outflow speed. This is true also for the terminal speed, which in plumes is lower by $\approx 10\%$ than in interplumes. However, Wang suggests plumes to contribute ‘only a modest fraction’ of the global high speed wind mass flux, because of their small filling factor. An analogous numerical integration model has been developed by Habbal et al. (1995): both Wang and Habbal et al. neglected the coupling between plumes and ambient plasma. An MHD model for plumes has been developed more recently by Del Zanna et al. (1997) and by Casalbuoni et al. (1999), who took into account the lateral pressure balance between the plume and the ambient plasma, but use a less sophisticated energy equation. These authors show that wind from plumes may be faster or slower than wind from the ambient hole, depending on the temperature difference and Alfvén wave flux assumed in the two regions.

The behavior of plumes which emerges from these works and the previously mentioned observations, is ambiguous. An analysis of their chemical composition may provide an additional proof that plumes do not contribute significantly to the fast wind. Widing & Feldman (1992) claim plumes to show a strong fractionation effect, which is absent in fast wind. Moreover, some recent observations seem to provide a stronger evidence in favor of the interplume plasma as the site where high speed wind originates.

Analyses of SUMER and UVCS data (see e.g. Hassler et al. 1997; Antonucci 1999; Wilhelm et al. 1998a; Giordano et al. 2000; Banerjee et al. 2000) have shown that the width of UV lines in interplumes is larger than in plume regions, hinting to interplumes as the site where energy is preferentially deposited and, possibly, fast wind emanates. A SUMER

analysis of the Ne VIII 770 Å line shifts in coronal holes has also revealed a weak outflow ($v \approx 3 \text{ km s}^{-1}$) which is absent in plumes (Wilhelm et al. 2000). Moreover, Giordano et al. (2000), from a Doppler dimming analysis of the O VI 1032 and 1037 Å lines at $1.7 R_{\odot}$, found an outflow speed between 0 and 65 km s^{-1} in plumes vs. an outflow between 105 and 150 km s^{-1} in interplumes. In qualitative agreement with these results, Patsourakos & Vial (2000), from a combination of Doppler shifts and Doppler dimming measurements of O VI doublet lines observed by SUMER, derive an interplume outflow speed of 67 km s^{-1} at $1.05 R_{\odot}$.

Although these analyses seem to support interplumes as sources of fast wind, they refer to different holes, observed at different times, and report on outflow values at only one level in the corona, rather than providing the outflow speed profile *vs.* height in interplumes, which is needed to understand the process of solar wind acceleration in the low corona. This paper aims at providing the outflow speed profile *vs.* height in interplume regions, between 1 and 2 solar radii. We will thus provide additional strong evidence supporting the idea that interplume regions are sources of the fast solar wind. The outflow velocity profile for O VI and H I ions in interplume areas will be derived from a Doppler dimming analysis of a unique data set, which combine SUMER and UVCS observations of a coronal hole. Moreover, we will show that plume observations may be reproduced on the basis of a simple model where a static plume is embedded in an ambient interplume plasma.

The paper is organized as follows. Section 2 illustrates the data set on which we base our analysis, while in the following section we describe the physical parameters (densities, electron and kinetic temperatures) used in our work. Section 4 discusses the outflow speed *vs.* altitude profile derived from the Doppler dimming analysis of the data and, in the following section, we show how plume observations can be interpreted on the basis of a static plasma. In section 6 we discuss our results and conclude our work by giving an empirical estimate of the heating rate per unit mass, for hydrogen and O VI ions.

2. Observations and Data Reduction

The observations discussed here were acquired by several instruments aboard SoHO on 1996 June 3 and were aimed at obtaining a high signal to noise ratio in the O VI 1032, 1037 and H I Ly α line profiles, in both plume and interplume regions of the north polar coronal hole. The pointing and areas observed with these instruments are shown in Fig. 1.

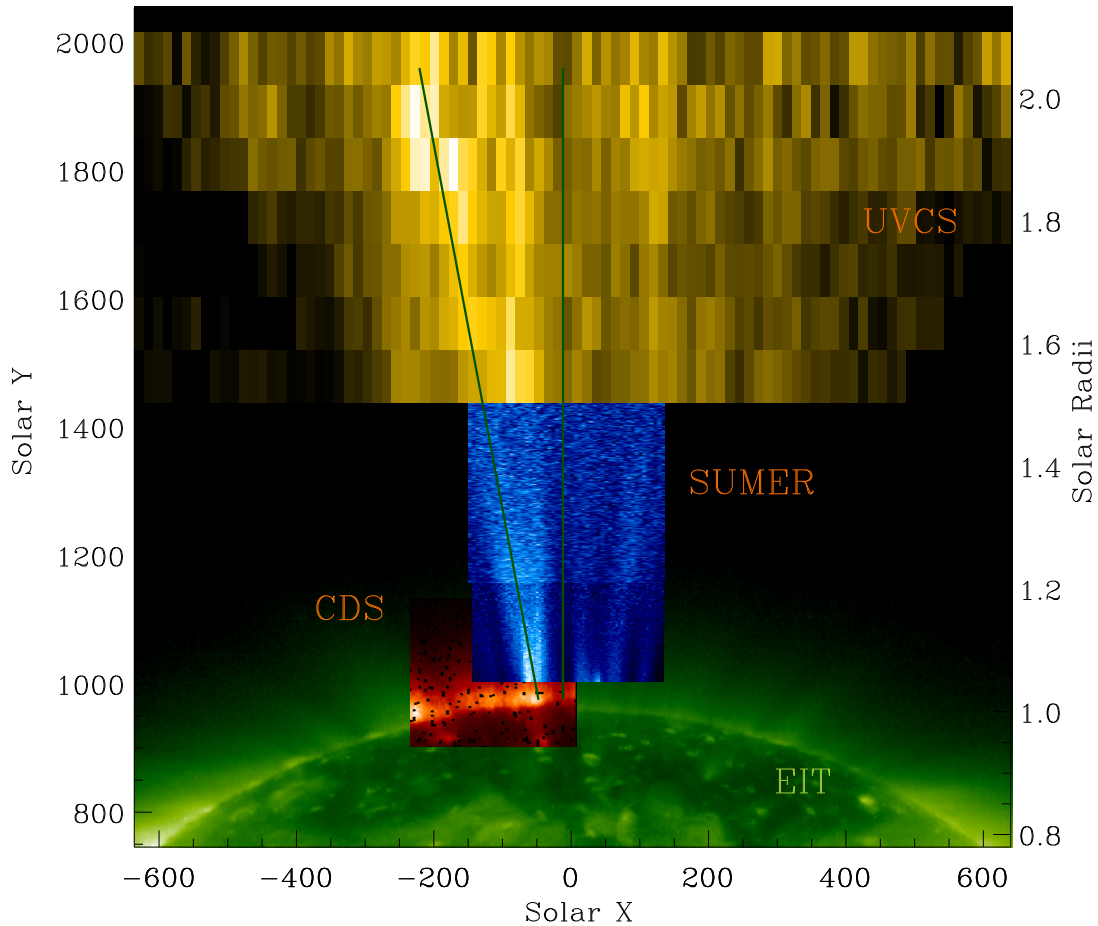


Fig. 1.— 1996 June 3 map of the north polar coronal hole as obtained using four of the instruments aboard SoHO. Strong plumes and interplume lanes can be identified in this diagram out to $2.0 R_{\odot}$ above the limb. An EIT (Delaboudinière et al. 1995) image in the Fe XII 195 Å line provides the disk image showing a well developed coronal hole. A CDS (Harrison et al. 1995) raster in the Mg IX 368 Å line shows the root of a large plume structure. A SUMER scan in the O VI 1032 Å line shows how the plume develops with altitude up to $1.5 R_{\odot}$. Above this altitude the structure of the coronal hole is obtained through seven spectra acquired in the O VI 1032 Å line with the UVCS slit normal to the solar radius. The contrast of the SUMER and UVCS maps was enhanced by dividing each map for its average intensity profile in the y -direction. The solid dark green lines indicate the regions selected as representative of plumes and interplume lanes.

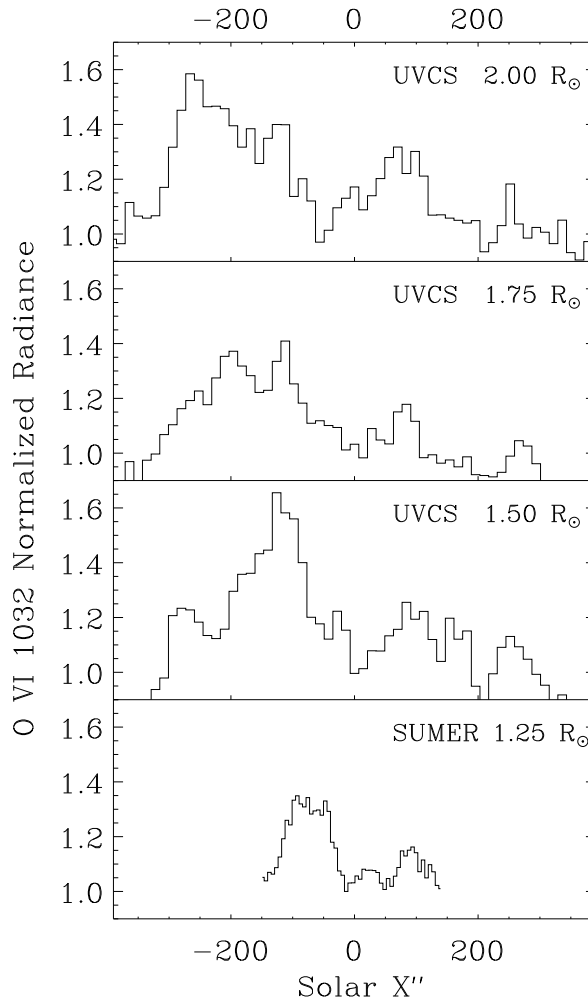


Fig. 2.— Horizontal cuts of the O VI 1032 data showed in Figure 1 at 1.25 (SUMER), 1.5, 1.75 and 2 (UVCS) solar radii. The intensity profiles have been normalized to the interplume values and that at 1.25 R_{\odot} has also been corrected for the stray light (see § 2.1).

2.1. SUMER Data

SUMER is a normal incidence spectrograph operating over the wavelength range ~ 500 to 1610 \AA (Wilhelm et al. 1995, 1997; Lemaire et al. 1997). The observations here discussed consist of two rasters of the north polar coronal hole obtained using the $4'' \times 300''$ slit. The first part is a raster scan consisting of 75 spectra obtained with an exposure time of 60 s. After each spectrum the slit was moved $3.76''$ westward covering an area of $\sim 278'' \times 300''$

centered at heliocentric coordinates $X = -4''$, $Y = 1150''$. An exposure time of 150 s was used for the second part, consisting of 52 spectra covering, with $5.65''$ steps, a region of $\sim 287'' \times 300''$ centered at $X = -6''$, $Y = 1300''$ (see Fig. 1). These rasters were aimed at obtaining high signal-to-noise line profiles in the plume and interplume regions above the limb out to $1.5 R_{\odot}$, over a total area of $\sim 280'' \times 470''$ (for further details see Banerjee et al. 2000). Data were reduced using various IDL routines from within the SUMER software tree.

SUMER spectral profiles were carefully fitted in order to obtain C II 1037, O VI 1032 and O VI 1037 Å line intensities. Despite the very high quality of the telescope mirror, the level of stray light is not negligible when observations of lines that are bright on disk are carried out above the limb (Lemaire et al. 1997). A chromospheric line, such as C II 1037, can be assumed not to have any coronal contribution and, hence, to be entirely due to stray light. The O VI 1032 stray component at a given altitude above the limb will be, hence, given by the product of the C II 1037 intensity at that altitude times the ratio of the disk-averaged O VI 1032 and C II 1037 line intensities. The above ratio was evaluated using observations at $1.8 R_{\odot}$, where the SUMER spectrum is entirely due to stray light. A stray light spectrum was, hence, builded and subtracted when fitting the O VI line profiles (see Banerjee et al. 2000 for further details). Scattered light was found to contribute the 15 and 36 % of the total interplume O VI 1032 line radiance at 1.1 and 1.25 solar radii, respectively.

Errors on line radiance were calculated through Poissonian statistics and, finally, their propagation in the O VI 1032/1037 line ratio was established. The small wavelength separation between the two O VI lines assures that the uncertainties in the radiometric calibration (15% for the present data: KBr coated A detector) do not affect the line ratio.

2.2. UVCS Data

The UltraViolet Coronagraph Spectrometer (Kohl et al. 1995) consists of three spherical telescope mirrors focusing co-registered images of the extended corona onto the three entrance slits of a spectrometer assembly consisting of two toric grating spectrometers – optimized for observations in Ly α (1145 - 1287 Å) and O VI (984 - 1080 Å), respectively – and a white light polarimeter measuring linearly polarized radiance in the 4500 - 6000 Å band.

In the observation here discussed 162 exposures of the corona above the north polar coronal hole were obtained with a 200 s integration time. During each exposure the entrance slits of the spectrographs were set tangent to the solar limb. A $300 \mu\text{m}$ wide slit was used to

record the O VI doublet while a 50 μm wide entrance was used for the H I Ly α observations. Exposures obtained at the same altitude were then combined to yield seven final pairs of spectra at altitudes ranging from 1.5 to 2.1 solar radii in steps of 0.1 R_{\odot} . Measurements of polarized radiation were also obtained at these altitudes by the white light channel (WLC). The pinhole feeding the WLC was pointing to a region that can be considered as average coronal hole. Spectra were reduced and calibrated using standard UVCS procedures. UVCS line profiles are shaped by the subresolution thermal and non-thermal motions of the observed plasma together with some instrumental effects that need to be evaluated and removed. Artificially broad line wings due to a detector effect that redistributes photon counts from the line core to the wings were corrected by convolving the observed profiles with a proper zero integral function (Kohl et al. 1997).

UVCS line profiles can also be modified by the chromospheric and transition region radiation scattered into the instrument. For each observed spectral line the amount of stray light at a given observing altitude was obtained, as a fraction of the line radiance on the disk, from data provided by Gardner (private communication). The Ly α disk radiance was obtained from SOLSTICE (Rottman, Woods, & Sparn, 1993) data while that of O VI 1032 was evaluated as explained in §3.3. The contribution of scattered light to the total interplume O VI 1032 and H I Ly α line radiance at 2.0 R_{\odot} was 4.8 and 7.8 %, respectively. The UVCS instrumental function turned out to scale with the width of the slit, approximately as given by the convolution of Gaussian profiles (Gardner et al. 1996). Thus, a stray light spectrum was built, convolved with the instrumental profile (accounting for the used slit) and subtracted when fitting the line profiles.

The contribution to the H I Ly α from the interplanetary hydrogen is about 3×10^7 ph $\text{cm}^{-2} \text{s}^{-1} \text{sr}^{-1}$ (Kohl et al. 1997), much smaller than the value we measure in interplume at 2 R_{\odot} (5.3×10^9 ph $\text{cm}^{-2} \text{s}^{-1} \text{sr}^{-1}$) and can be considered negligible.

3. Data Analysis and Modeling

After selecting a plume and an interplume region by identifying the brightest and darkest features within the imaged area (see Figs. 1 and 2), data within these regions were binned over 5×15 pixels (in the X and Y directions, respectively) for the first (lower) SUMER scan, and over 4×30 pixels for the second SUMER scan. Final UVCS spectra were averaged to obtain line profiles at 1.5, 1.6, 1.75 (average of data taken at 1.7 and 1.8 R_{\odot}) and 2.0 (average of data taken at 1.9, 2.0 and 2.1 R_{\odot}) solar radii. In such a way, O VI line profiles were determined at 19 different locations above the solar limb for both plume and interplume regions. These observations allow us to study these structures from the disk up to two solar

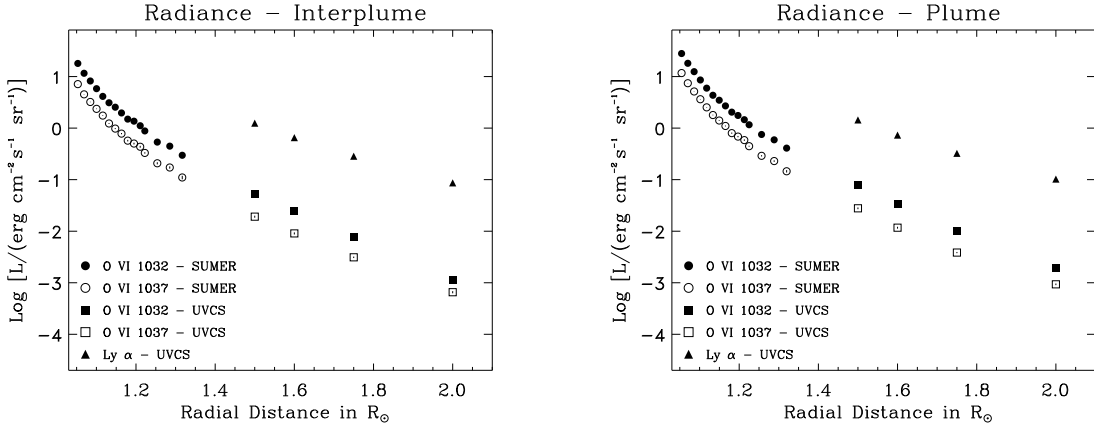


Fig. 3.— O VI 1032, 1037 Å and H I Ly α 1215 Å line radiances as a function of altitude along the interplume (left panel) and plume (right panel) regions of the north polar coronal hole indicated with solid green lines in Fig. 1. Filled (open) circles and squares represent the O VI 1032 (O VI 1037) line radiances as measured with SUMER and UVCS, respectively. H I Ly α radiances measured with UVCS are indicated by filled triangles.

radii following an intensity drop-off of the O VI lines of about four order of magnitude, as shown in Fig. 3. Moreover, at 1.5, 1.6, 1.75 and 2.0 solar radii, also UVCS H I Ly α profiles are available (see Fig. 3).

For allowed transitions from the ground level of ions without metastable levels (such as Li-like and H-like ions), only the ground level g and the excited upper level u responsible for the line emission are important in the calculations of the line intensity and the transition is, hence, well described by a two level atomic model. This is the case of the O VI 1032 and 1037 Å and the H I Ly α lines. In the solar corona, these lines are formed by electron impact excitation (collisional component) and by resonant scattering (radiative component) of the radiation coming from the disk (Gabriel 1971; Withbroe et al. 1982; Kohl & Withbroe 1982; Noci et al. 1987; Noci & Maccari 1999). Very schematically,

$$\begin{aligned}
 I_{obs} &= I_{Coll.} + I_{Rad.} = 0.83 \frac{\Delta E_{gu}}{4\pi} A_{el} \times \\
 &\times [\langle q(T_e)R(T_e)N_e^2 \rangle + B_{gu} \langle D(f(\mathbf{v}), I_{\odot})R(T_e)N_e \rangle]
 \end{aligned}
 \tag{1}$$

where ΔE_{gu} is the energy of the transition from g to u , A_{el} is the element abundance relative to hydrogen, N_e the electron number density, $q(T_e)$ the collisional excitation rate coefficient, B_{gu} is the Einstein absorption coefficient, $R(T_e)$ is the ionic fraction calculated in ionization equilibrium, and 0.83 is the value of the hydrogen to electron number density ratio for a

fully ionized plasma with 10% of helium. The quantities in brackets $\langle \dots \rangle$ are integrated along the line of sight (LOS). $D(f(\mathbf{v}), I_{\odot})$ accounts for Doppler dimming and geometrical dilution factors and is a function of the ion speed distribution $f(\mathbf{v})$ and of the exciting line radiance distribution I_{\odot} over the solar disk. This term needs to be integrated, for each point along the LOS, over the solid angle subtended by the Sun (for a more detailed description of the different terms of Eq. 1 see Cranmer et al. 1999 and Zangrilli et al. 2002 and references therein). The speed distribution $f(\mathbf{v})$ can be represented by an anisotropic bi-Maxwellian with independent, most probable $1/e$ speeds, v_{\parallel} and v_{\perp} that are parallel and orthogonal, respectively, to the magnetic field lines (Li et al. 1998). The speed distribution $f(\mathbf{v})$ also depends on the outflow ions speed w along the magnetic field lines. v_{\parallel} and v_{\perp} can be expressed as kinetic temperatures T_{\parallel} and T_{\perp} through the relation $v^2 = 2kT/m$.

In these conditions the intensity of the resonantly scattered component of a coronal line is a function of the speed components along the magnetic field lines (w and v_{\parallel}) via the Doppler dimming of the disk’s incident profile in the frame of reference of the outflowing ions (Beckers & Chipman 1974). This means that, knowing the atomic parameters of the transition, the physical characteristics of the emitting plasma (such as chemical composition, electron density, electron temperature and the v_{\parallel} and v_{\perp} distributions) and the disk radiance, we are able to find the outflow speed profile that reproduces our observations. Many of these parameters can be constrained by our observations and/or through values given in the literature, while others are free parameters which we vary in order to explore the dependence of the outflow speed on the physical properties of the emitting region.

In this context, the ratio of the O VI 1032 to O VI 1037 Å line radiances (hereafter R_{OVI}) is a very powerful tool in investigating the outflow speed profile of the O VI ions (Noci et al. 1987). In fact, R_{OVI} is independent of the elemental abundance and is practically insensitive to the electron temperature T_e (Li et al. 1998), both parameters being largely uncertain in the solar corona. Moreover, differential departures from the expected ionization equilibrium between the ions are prevented when considering the ratio of lines belonging to the same ionization stage (Mariska 1992).

At transition region electron densities ($10^9 - 10^{10} \text{ cm}^{-3}$), $I_{\text{Coll.}} \gg I_{\text{Rad.}}$ and the ratio reduces to that of the oscillator strengths $\simeq 2$, as shown by on-disk observations. If only the radiative components would be present, the ratio would be close to 4 (depending on the value of T_{\perp} and T_{\parallel} , see e.g. Cranmer et al. 1999; Li et al. 1998) for a static plasma ($w = 0$). Above the solar limb, due to the electron density drop-off with altitude, $I_{\text{Coll.}}$ and $I_{\text{Rad.}}$ may be comparable and the ratio is sensitive to the outflow speed. For outflow speeds smaller than 150 - 200 km s^{-1} we anticipate, if the same outflow speed were present in both the plume and interplume, the denser plume to be characterized by a lower ratio than the interplume

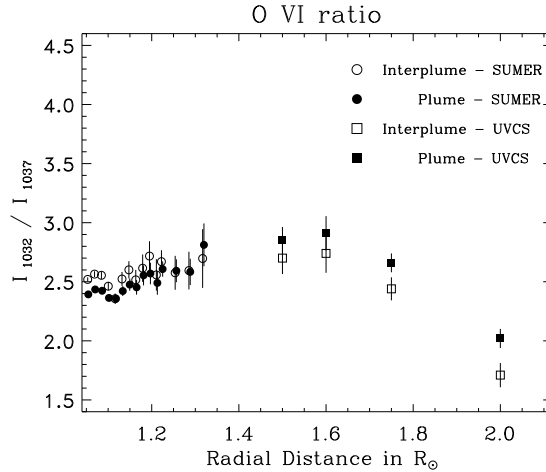


Fig. 4.— O VI 1032 to O VI 1037 line radiance ratio (R_{OVI}) as observed along the selected plume and interplume regions of the north polar coronal hole. Filled circles (squares) refer to SUMER (UVCS) measurements in the plume, while open circles (squares) refer to SUMER (UVCS) measurements in the interplume.

(being $I_{Coll} \propto N_e^2$). In Fig. 4, R_{OVI} measured in both the plume and the interplume region is shown. At altitudes below $1.2 R_{\odot}$, the SUMER data show the plume to be characterized by a smaller value of R_{OVI} than interplume, while the opposite behaviour is evident at higher altitudes in the UVCS data. This may be indicative of a higher outflow speed in interplume than in the plume, hinting at these less dense and cooler regions as those from where the fast solar wind emanates. However, for outflow speeds above $150 - 200 \text{ km s}^{-1}$, the “pumping” by the nearby C II 1037.0182 Å line, makes this conclusion not straightforward. Hence, we want first to model our data in order to determine the outflow profile in the interplume and, once this is accomplished, verify whether our plume observations can be reproduced by a static plume embedded in an interplume medium characterized by the previously determined outflow profile. The outflow profile in interplume will be found by reproducing the observed R_{OVI} and the O VI 1032 and O VI 1037 line intensity. H I Ly α , almost totally ($\sim 99\%$, Raymond et al. 1997) formed by resonant scattering, allows us to evaluate also the H I outflow speed. However, because of the use of the electron temperature in the $R(T_e)$ calculations, the derived values are more uncertain.

3.1. Electron densities

Both radiative and collisional components are strongly dependent on the electron density (N_e). As outlined in § 2.2, our UVCS observations include also polarized radiation measurements that allow us to determine the electron density between 1.5 and 2.1 solar radii for the average coronal hole (van de Hulst 1950). Results are shown in Fig. 5 as filled squares. At higher altitudes the same technique was applied to LASCO (Brueckner et al. 1995) C 2 data, thus allowing us to extend our measurements above 2.5 R_\odot . The directions outlined by the solid green lines in Fig. 1 were roughly followed outward on LASCO images to obtain densities in plumes (solid line) and interplumes (dash-dotted line). Unfortunately, we had no way to derive electron densities from our data below 1.5 R_\odot . Hence, N_e values below 1.5 R_\odot were taken by Wilhelm et al. (1998a) who measured the electron density profiles in plume and interplume below 1.3 R_\odot . Electron densities in coronal holes have been evaluated by several authors (e.g. Kohl et al. 1998; Wilhelm et al. 1998a; Banerjee et al. 1998; Doschek et al. 1997; Fisher & Guhathakurta 1995). However, in the present analysis only data obtained in 1996 (*i. e.* closer in time to our data) were used to complement our measurements. The adopted density profiles in plumes and interplumes are shown with thick dotted and dashed lines, respectively.

3.2. Ion and electron temperatures

The determination of the electron temperature profile in the solar corona is particularly controversial. The discrepancy between the electron temperatures obtained in the inner corona through spectroscopic diagnostics (see e.g. Wilhelm et al. 1998a) and the values deduced from ion charge composition measurements obtained *in-situ* in the solar wind by Ulysses (see e.g. Ko et al. 1997), is well known (see e.g. Esser & Edgar 2000). Spectroscopically derived T_e values never exceed 10^6 K in the range 1.05–1.3 R_\odot . Values by Wilhelm et al. (1998a) are particularly accurate since they use the ratio of lines of the same ion (Mg IX 706/750), thus avoiding problems with elemental abundances, ionic fractions, and differential flow speeds between different ions (Esser & Edgar 2000). The closeness in wavelength minimize also the errors arising from the instrument calibration. Moreover, these are the only measurements providing the T_e *versus* height profiles in plume and interplume. At higher altitudes, an electron temperature of 1.075 MK is given by Wimmer-Schweingruber et al. (1998) from *in situ* measurements of the O VII/O VI ion ratio in fast wind streams. We assume as electron temperature profiles in plume and interplume those obtained by Wilhelm et al. (1998a) below 1.3 R_\odot . Above this altitude the temperature was assumed to remain constant. The O VI and H I ionic fractions were then obtained from calculations by Arnaud

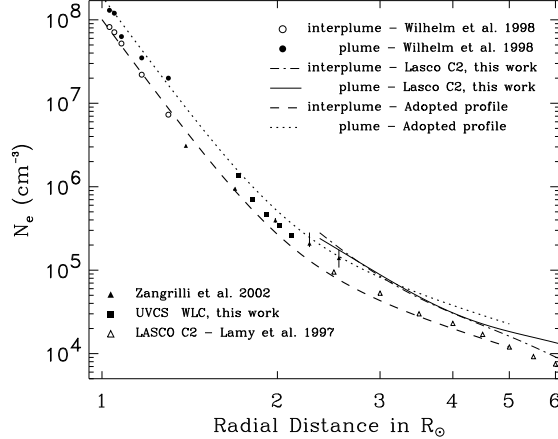


Fig. 5.— Electron density as a function of altitude in polar coronal holes. Measurements obtained in interplume: Wilhelm et al. 1998a (*open circles*), LASCO C 2 (*thin dash-dotted line*, this work). Measurements obtained in plumes: Wilhelm et al. 1998a (*filled circles*), LASCO C 2 (*thin solid line*, this work). Measurements obtained without distinguishing between plume and interplume: Zangrilli et al. 2002 (*filled triangles*), Lamy et al. 1997 (*open triangles*), UVCS White Light Channel (*filled squares*, this work). Thick dotted and dashed lines represent the adopted density profiles in plumes and interplumes, respectively.

& Rothenflug (1985) and Mazzotta et al. (1998), respectively.

For the observations discussed here, we can assume the magnetic field lines to be perpendicular to the line of sight. This allows us to identify T_{\perp} with the effective temperature T_{eff} defined through the equation:

$$v_{1/e}^2 = \frac{2kT_{eff}}{m} \quad (2)$$

where m is the ion mass and $v_{1/e}$ is the Doppler width (in km s^{-1}) or most probable speed of the unresolved (thermal + non-thermal) motions distribution, given by

$$v_{1/e} = \frac{\Delta\lambda_D}{\lambda}c, \quad (3)$$

where λ is the wavelength, c the speed of light, and $\Delta\lambda_D$ the measured half width of the line at $1/e$ of the peak intensity. We find line widths in interplume to be greater than those observed in plume, as already found by many authors (Banerjee et al. 2000; Antonucci 1999; Giordano et al. 1997). T_{\perp} profiles for both plume and interplume were obtained from our data (see Fig. 6).

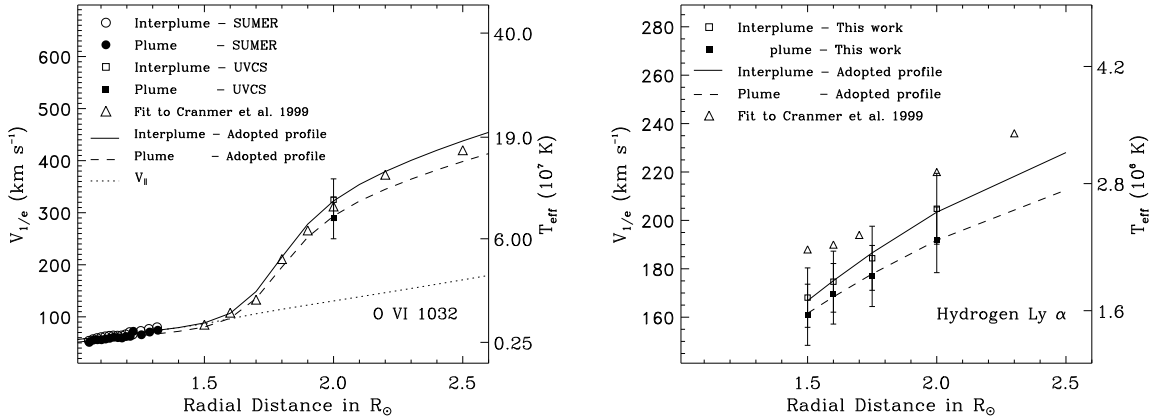


Fig. 6.— Variation of the O VI 1032 (*left panel*) and H I Ly α (*right panel*) most probable speed $v_{1/e}$ with height along the selected plume and interplume regions. Filled circles (squares) represent SUMER (UVCS) measurements in the plume, while open circles (squares) represent SUMER (UVCS) measurements in the interplume. Open triangles show the fit to the data obtained by Cranmer et al. (1999) for an average coronal hole plasma. Solid and dashed lines indicate the adopted $v_{1/e}$ profiles in interplume and plume, respectively. On the right axis is shown the effective temperatures obtained through Eq. 3. On the left panel, the dotted line gives the profile of the most probable speed along the magnetic field lines (V_{\parallel}) that allows us to mimic the O VI data in the semi-isotropic case (see §4).

The temperature parallel to the magnetic field lines, T_{\parallel} , can not be directly measured. In these conditions it is reasonable to explore two extreme cases: $T_{\parallel} = T_e \ll T_{\perp}$ that assumes ions to be in thermal equilibrium with electrons along the magnetic field lines (fully anisotropic case), and $T_{\parallel} = T_{\perp} \gg T_e$ (fully isotropic case).

3.3. Disk radiance and elemental abundance

During June 1996 the Sun was at its minimum of activity with no active regions on the disk. In these conditions the disk can be thought as uniformly bright with a radiance equal to the disk-averaged line radiance. For the H I Ly α this value was obtained from SOLSTICE data. For the O VI 1032 Å line, I_{\odot} was evaluated assuming a $1/\cos(\theta)$ center-to-limb line intensity variation (Wilhelm et al. 1998) and adopting a radiance at disk centre of 300 erg cm $^{-2}$ s $^{-1}$ st $^{-1}$, obtained from a disk centre SUMER scan obtained on 1996 June 4 over a 40'' \times 120'' region.

Because we want to reproduce also the O VI line radiances, we need to know the oxygen

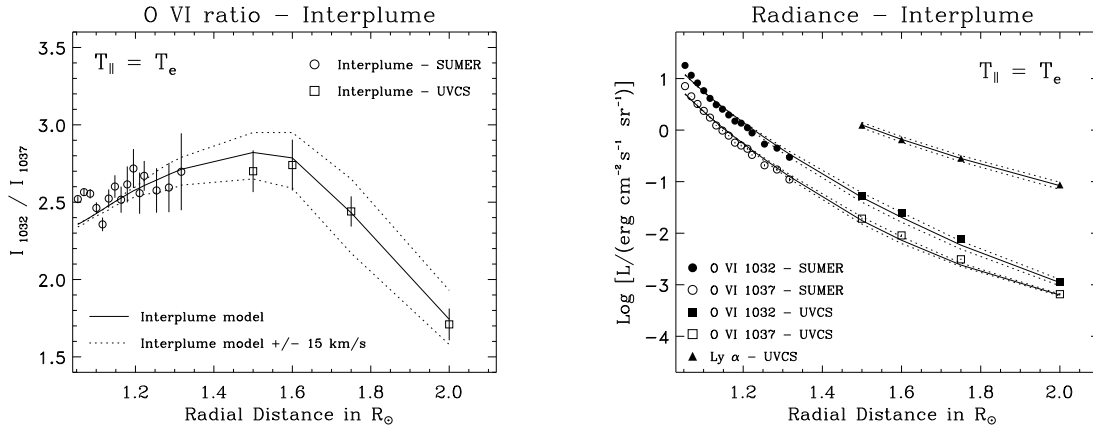


Fig. 7.— Model solution for interplume conditions in the anisotropic case ($T_{\parallel} = T_e$). The O VI 1032 to O VI 1037 line ratio (left panel) and their radiances (right panel) in interplume are shown. The line radiance of the H I Ly α line is also shown on the right panel. On both panels, solid lines represent the anisotropic solution, while the O VI line ratio and the line radiances obtained by changing the outflow speed of $\pm 15 \text{ km s}^{-1}$ are shown with dotted lines.

abundance with respect to hydrogen in both plume and interplume. Solar abundances, however, are poorly determined (see von Steiger et al. 2001; Raymond et al. 2001; and reference therein). Using the adopted electron density and temperature profiles it is possible to reproduce, through Eq. 1, the O VI 1032 to 1037 observed line radiance ratios below $1.2 R_{\odot}$ assuming a negligible outflow speed. In these conditions ($w \sim 0$), O VI line radiances depend on the elemental abundance only (once the density and temperature profiles have been fixed). We found that the observed line radiances below $1.2 R_{\odot}$ can be reproduced adopting an oxygen abundance of 8.5. We assume plume and interplume to have the same abundance and we will discuss later this assumption.

4. Outflow speed in interplume lanes

Using the adopted interplume T_e and N_e profiles and an oxygen abundance of 8.5, we found the outflow speed profiles capable of reproducing the observed interplume O VI line ratios as well as the observed O VI and H I Ly α line radiances. Outflow speed profiles were determined by an iterative procedure that calculates the line radiances at all the observed heights. Zero outflow speed was assumed in the first step, then the speed was increased in 3 km s^{-1} steps until the calculated radiances and O VI line ratio matched the observed ones.

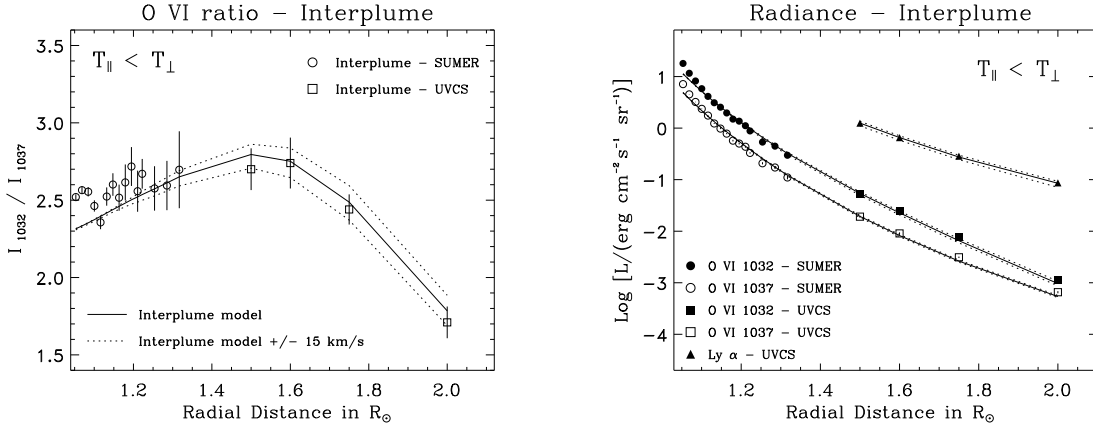


Fig. 8.— Model solution for interplume conditions in the semi-isotropic case ($T_{\perp} > T_{\parallel} > T_e$). The O VI 1032 to O VI 1037 line ratio (left panel) and their radiances (right panel) in interplume are shown. The line radiance of the H I Ly α line is also shown on the right panel. On both panels, solid lines represent the semi-isotropic solution (isotropic for H I atoms), while the O VI line ratio and the line radiances obtained by changing the outflow speed of $\pm 15 \text{ km s}^{-1}$ are shown with dotted lines.

Figs. 7 and 8 give the R_{OVI} ratio and the O VI and H I line radiances vs. height, calculated on the basis of the outflow profiles derived as illustrated above, superposed onto the observed values for, respectively, the anisotropic and semi-isotropic case. It is worth noticing that, in the fully isotropic case ($T_{\parallel} = T_{\perp}$) there is no solution capable of reproducing the O VI data, as already found by Cranmer et al. (1999). Hence the solution we show in Figure 8 is for the highest T_{\parallel} that allows us to mimic the data (see left panel of Fig. 6). A fully isotropic solution was, instead, found for H I ions. The calculated values reproduce observations remarkably well, over the four order of magnitude covered by the data. However, because both the isotropic and anisotropic cases mimic the data, we cannot point to one of the two solutions as representative of the physical properties of interplumes. This ambiguity is shared also by models for the average corona.

Figure 9 shows the O VI ion outflow speed vs. height profile (left panel), from 1.05 to 2 solar radii, for the anisotropic (open symbols) and semi-isotropic (filled symbols) case, together with Cranmer et al. (1999) solutions for an average corona for the two cases. Analogously, the right panel of Fig. 9 gives the H I outflow speed vs. height profile, and the Cranmer et al. profiles, for the isotropic and anisotropic conditions, at altitudes above 1.5 R_{\odot} .

Observed line radiances are affected by uncertainties that propagate onto the derived

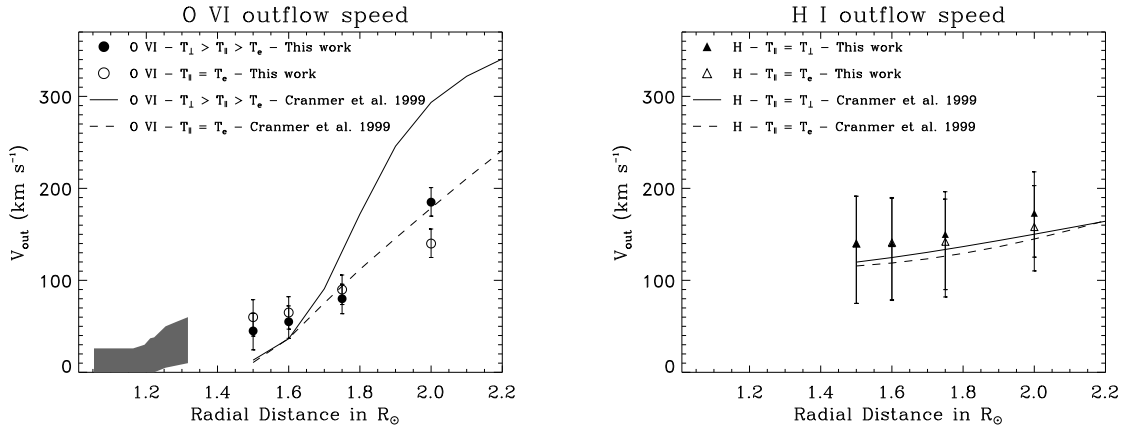


Fig. 9.— O VI ions (left panel) and H I atoms (right panel) outflow speed in interplume lanes between one and two solar radii. Filled symbols refer to the semi-isotropic models (fully isotropic for H I ions), while open symbols indicate the results for the anisotropic model. The shaded area between 1.05 and 1.3 solar radii indicates speed values compatible with SUMER data (see text). The outflow speed profiles found by Cranmer et al. are shown for comparison.

outflow speed values. Figs. 7 and 8 show the O VI line ratio and the line radiances obtained by changing the obtained outflow speeds by $\pm 15 \text{ km s}^{-1}$ (dotted lines). This value has been adopted as representative of the errors due to the observational uncertainties on the measured line radiances. Moreover, there are uncertainties also on the adopted density and temperature profiles and on the adopted disk radiance. The errors on the derived outflow speed arising by a 20 % uncertainty on the electron density, a 25% uncertainty on the electron temperature and a 15 % uncertainty on the disk radiance were also evaluated and summed in quadrature to the observational errors.

For O VI ions (left panel of Fig. 9), in the range $1.05 \leq R/R_{\odot} \leq 1.3$, we chose to show a shaded area, which includes speed values that are compatible with the data, rather than giving a precise profile. Hence, even a static plasma might be compatible with the data. This happens because Doppler dimming is not very sensitive to speeds as low as those in the shaded region, and we are unable to give precise values of the O VI outflows. However, above $1.3 R_{\odot}$, unless a flow is introduced, observations cannot be reproduced.

We postpone further comments on the outflow profiles of Figure 9 to §6 and move on to check whether a static plume, immersed in the interplume ambient we derived, is compatible with the line radiances and O VI line ratio observed in plumes.

5. The plume model

A realistic attempt to model our plume observations requires a combination of plume and interplume emissivities along the line of sight. A mixed plume-interplume model has been, hence, created assuming a single plume with no outflowing plasma embedded in interplume plasma outflowing with the speed profiles determined in the previous Section. Because plumes expand superradially with altitude (DeForest et al. 2001), the line of sight fraction occupied by the plume was estimated assuming a magnetic flux tube with an area growing with altitude as:

$$A(R) = A(R_\odot) \left(\frac{R}{R_\odot} \right)^2 f(R) \quad (4)$$

where $f(R)$ is the superradial expansion factor given by Kopp & Holtzer (1976) and written as:

$$f(R) = 1 + (f_{max} - 1) \left(\frac{1 - \exp[R_\odot - R]/\sigma_1]}{1 + \exp[R_1 - R]/\sigma_1]} \right) \quad (5)$$

with $f_{max} = 6.5$, $R_1 = 1.5 R_\odot$, and $\sigma_1 = 0.6 R_\odot$. Assuming rotational symmetry around the polar axis, the length along the LOS occupied by the plume at an altitude R can be written from Eq. 4 as:

$$2l(R) = 2l(R_\odot) \left(\frac{R}{R_\odot} \right) f(R)^{1/2} \quad (6)$$

where $l(R_\odot)$ is the radius of the plume at the solar surface. This model is able to reproduce our plume observations assuming $l(R_\odot) = 0.018$ and $0.016 R_\odot$ for O VI and H I Ly α , respectively.

Eq. 6 gives, at $R = 1.16 R_\odot$, a plume radius of ≈ 18000 km, in agreement with a radius of ≈ 20000 km, that we measure from our data. At an altitude of $2 R_\odot$, where UV data do not allow a reliable estimate of the plume radius, Eq. 6 yields a radius of 51000 km, which favorably compares with a radius of 61000 km, measured on Spartan data (Fisher & Guhathakurta, 1995). At the plume base, the value we adopted is consistent with the diameter of the observed plume structure as derived from the CDS scan in the Mg IX 368 \AA line.

Results for our “mixed” model are given in Figs. 10 and 11, for the anisotropic and semi-isotropic cases, respectively. Analogously to what we did for Figs. 7 and 8, we show in the left panels the observed and simulated O VI doublet line ratio vs. altitude and, in the right panels, the observed and simulated O VI 1032, 1037 and H I Ly α line radiances in plume. On the left panels we also give the results of a model where a static plasma representative of plume conditions occupies the entire LOS (i.e. a pure plume model) together with the interplume models previously derived, to show how different assumptions affect results.

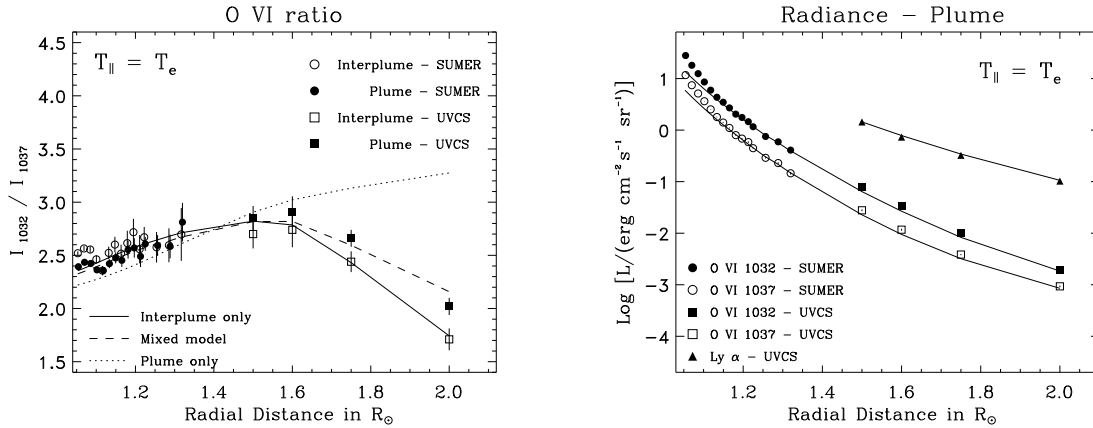


Fig. 10.— Model solutions for plume observations in the anisotropic case ($T_{\parallel} = T_e$). The O VI 1032 to O VI 1037 line ratios in plume (filled symbols) are shown on the left panel together with those observed in interplume (open symbols) as comparison. A dashed line represents the mixed model built assuming a static plume embedded in an interplume outflowing plasma. The results for interplume conditions (already shown in Fig. 7) and for a plume extending over the whole LOS are also shown with solid and dotted lines, respectively. On the right panel, the line radiance of the O VI lines and of the H I Ly α line in the plume are shown together with the radiances computed assuming a static plume embedded in an interplume outflowing plasma (solid lines) in the anisotropic case.

Independently of the temperature behavior (isotropic or non-isotropic), the mixed model simulates quite well the behaviour of the line ratio and radiances observed in plumes, in the altitude range of our observations. Although we cannot claim the solution to be unique, as discussed in the following Section, our simulations show that a static plume model, embedded in the interplume plasma whose characteristics have been previously described, is fully capable of reproducing the observations. This result provides additional evidence in favor of interplumes as sources of the nascent solar wind.

6. Discussion and Conclusion

In the last few years a number of papers addressed the problem of the nascent fast wind characteristics (see e.g. Cranmer et al. 1999; Antonucci et al. 2000; Zangrilli et al. 2002, for the wind properties from UVCS data, and Hassler et al. 1999; Banerjee et al. 2000; Wilhelm et al. 2000, for wind properties from SUMER data). However, the behavior of the solar wind in the altitude range between 1 and 1.5 solar radii remains largely unknown. This

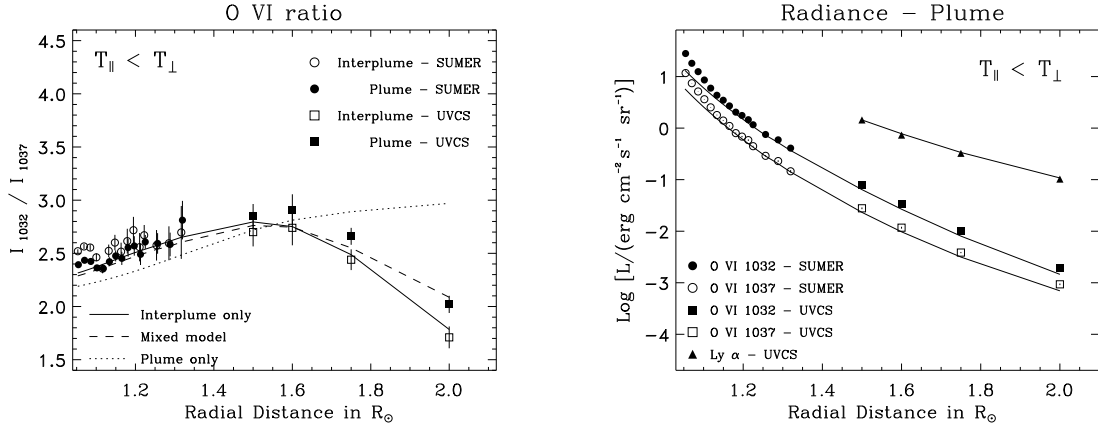


Fig. 11.— Model solutions for plume observations in the semi-isotropic case ($T_{\perp} > T_{\parallel} > T_e$). The O VI 1032 to O VI 1037 line ratios in plume (filled symbols) are shown on the left panel and compared with those observed in interplume (open symbols). A dashed line represents the mixed model built assuming a static plume embedded in an interplume outflowing plasma. The results for interplume conditions (already shown in Fig. 8) and for a plume covering the whole LOS are also shown with solid and dotted lines, respectively. On the right panel, the line radiance of the O VI lines and of the H I Ly α line in the plume are shown together with the radiances computed assuming a static plume embedded in an interplume outflowing plasma (solid lines) in the semi-isotropic case.

height interval is very relevant for our understanding of the process of wind acceleration: the identification of the source region of the fast wind and the knowledge of the wind speed at these low levels is crucial for the development of any realistic wind model.

The results presented in this paper provide strong evidence in favor of interplume regions as sources of fast wind streams: we have shown that the physical parameters of the interplume ambient are compatible with the presence of an outflowing plasma, while plume observations can be explained on the basis of a static plume, embedded in interplume regions. We also provided, for the first time, a profile of the plasma outflow speed vs. height, between 1 and 2 solar radii, for O VI ions. We point out that our results are consistent with Hassler et al. (1999) or Wilhelm et al. (2000) findings, once their LOS flows are converted to radial outflows. On the other hand, we do not find flows as high as those reported by Patsourakos and Vial (2000) which, however, are derived using a significantly lower ambient electron density than in our case. In any case, we caution the reader that the values of the outflow speed at levels below $1.5 R_{\odot}$, have to be considered only as representative of real values. Up to $\approx 1.2 R_{\odot}$ an outflow of a few km s^{-1} reproduces our observations as well as a static plasma, because Doppler dimming is insensitive to such low outflows. Hence, we have indicated with

a shaded area the range of values consistent with our data: outflow values lie within that region, but we cannot identify the precise outflow speed gradient.

At altitudes larger than $1.5 R_{\odot}$, the H I and O VI ions outflow profiles shown in Fig. 9 are consistent with those given by other authors. The figure gives, as a reference, the profiles derived by Cranmer et al. (1999) for an average corona (i.e. averaged over dense plumes and low density interplume regions). The most obvious difference between the O VI outflow profile we inferred and that of Cranmer et al. is in the value of the outflow speed at $1.5 R_{\odot}$, where we derived an O VI speed of $\approx 50 \text{ km s}^{-1}$. At higher levels, our data reproduce the outflow speed gradient derived by Cranmer et al. in their anisotropic model. We may conclude that our results indicate that plasma starts being heated and accelerated outwards at lower levels than anticipated by models which did not separate the plume and interplume components of the coronal plasma.

As we said, we are unable to point to the real outflow speed vs. height profile at very low levels, because of the range of values of the outflow speed that reproduce, within the uncertainties of measurements, our observations. However, plasma is being accelerated at low levels and this provides a strong indication for modelers: any heating process (or, equivalently, any heating function) should start to heat and accelerate the plasma below 1.5 solar radii. In order to give modelers some information about the coronal heating rate at levels below 2 solar radii we can use a simplified energy equation, where Coulomb collision terms are neglected (Tu & Marsch 1999):

$$Q = v_{out} \left(\frac{dv_{1/e}^2}{dR} + v_{1/e}^2 \frac{2}{R} \right). \quad (7)$$

Because collision terms are negligible only above $\sim 1.7 R_{\odot}$, in Fig. 12 we give an estimate of the heating rate, per particle, for O VI ions (filled circles) and H I atoms (filled triangles) in interplume regions, from our obtained outflow speeds (v_{out}) and measured effective temperatures ($v_{1/e}$) at 1.75 and 2 solar radii. These values can be complemented with the heating rates calculated by Tu & Marsch (1999) at $3 R_{\odot}$, from UVCS data for a coronal hole plasma averaged over plume and interplume regions (open symbols). In the inner corona, at least to distances of two solar radii, protons and neutral hydrogens are well coupled (Withbroe et al. 1982; Olsen, Leer & Holzer 1994; Allen, Habbal & Hu 1998) so that H I atoms can be used as a proxy for protons. Our results can be also compared with the heating rates obtained by Hu et al. (2000) in a four-fluid solar wind model based on the dissipation of high frequency ion cyclotron waves. These authors made the calculation with (Case A) and without (Case B) including the dispersive effect of minor ions for both O VI ions and protons. A substantially good agreement can be seen between our observational results and the numerical models, particularly for the O VI ions.

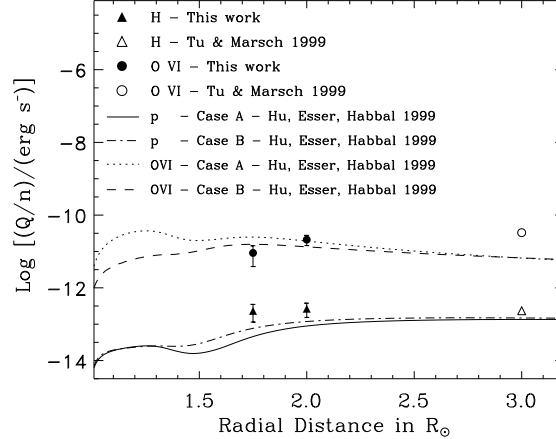


Fig. 12.— O VI ions (circles) and protons (triangles) heating rates as inferred from Eq. 7. Filled symbols represent values derived from our data, while the values provided by Tu & Marsch (1999) at $3 R_{\odot}$ are represented with open symbols. Solid and dot-dashed lines indicate the heating rate profiles obtained by Hu et al. (2000) for protons with (Case A) and without (Case B) the dispersive effect of the minor ions, respectively. Dotted and dashed lines indicate the heating rate profiles obtained by Hu et al. (2000) for O VI ions with (Case A) and without (Case B) the dispersive effect of the minor ions, respectively.

At lower altitudes we are not able to calculate the heating rates due to the growing importance of the Coulomb terms. However, the Hu et al. (2000) calculations provided also outflow speed and $v_{1/e}$ profiles that can be compared with our results at all heights. Figure 13 shows (left panel) the O VI outflow profiles obtained for both semi-isotropic (filled circles) and anisotropic conditions (open circles) together with the outflow speeds calculated by Hu et al. (2000) with (Case A, solid line) and without (Case B, dashed line) the dispersive effect of the minor ions. Similarly, the right panel of Figure 13 compares the results for H I ions with those obtained by Hu et al. (2000) for protons.

Figure 14 compares our measured $v_{1/e}$ values with those provided by the model. The good agreement between the model and the observations is obvious, and shows that predictions from the theory of heavy ion acceleration by ion-cyclotron waves are consistent with observational results. However, further work is probably required to explain H/proton acceleration, which is possibly confined to lower altitudes than those where oxygen ions are being accelerated and may have a steeper speed profile than suggested by theoretical models.

Before concluding, we like to comment about our choice of the oxygen abundance in plumes. As we mentioned in the Introduction, Widing & Feldman (1992) claim to observe a

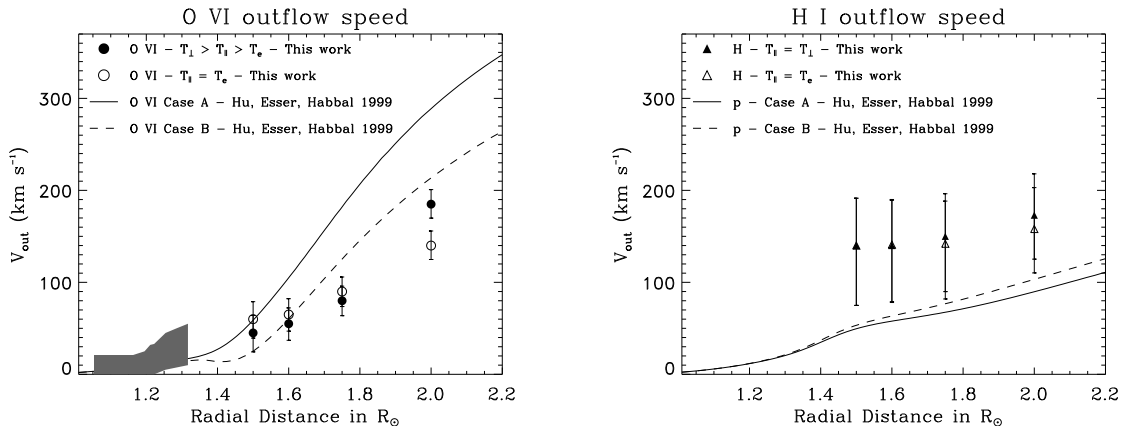


Fig. 13.— O VI ions (left panel) and H I atoms (right panel) outflow speed in interplume lanes between one and two solar radii. Filled symbols refers to the semi-isotropic models (fully isotropic for H I ions), while open symbols indicate the results for the anisotropic model. The shaded area between 1.05 and 1.3 solar radii indicates speed values compatible with SUMER data. Outflow speed profiles obtained by Hu et al. (2000) for O VI ions and protons with (Case A) and without (Case B) the dispersive effect of the minor ions are shown using solid and dashed lines, respectively.

strong fractionation effect in plumes, which can possibly be interpreted in terms of an increase of the oxygen abundance in plumes. Here, instead, we chose to adopt the same oxygen abundance both in plumes and interplumes, on the ground that the interplay between oxygen abundance and plume filling factor makes any choice completely arbitrary and irrelevant for our conclusions. The observed O VI line ratio and the intensities of the individual doublet lines can be reproduced by a static plume ambient, independently of the value of the oxygen abundance, a higher value implying only a lower plume filling factor along the line of sight. Moreover, in a very recent work, Del Zanna et al. (2002) find that plumes do not show any FIP effect and are characterized by elemental abundances close to photospheric values.

Acknowledgments

The work of L.T. and G.P. has been supported by ASI (Italian Space Agency) and MIUR (Italian Ministry of University and Scientific Research). SoHO is a mission of international cooperation between ESA and NASA. Authors are particularly grateful to Ruth Esser for providing the model data published by Hu et al. (2000). We would also like to thank the anonymous referee for very useful comments and suggestions.

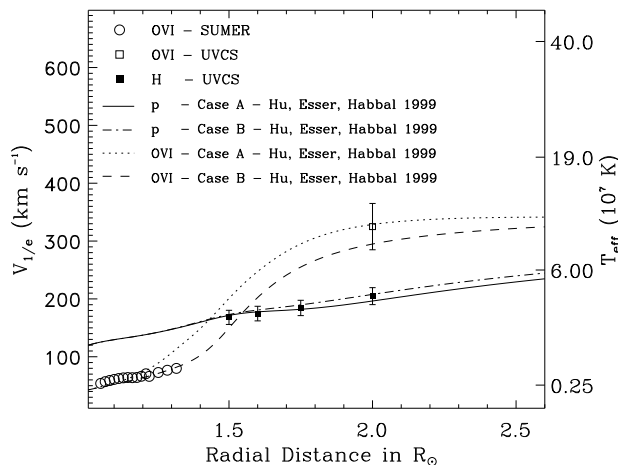


Fig. 14.— Variation of the O VI 1032 and H I Ly α most probable speed $v_{1/e}$ with height along the selected interplume region. Open circles (squares) represent SUMER (UVCS) measurements in O VI, while filled squares represent UVCS measurements in the H I Ly α . Solid and dot-dashed lines indicate the $v_{1/e}$ profiles obtained by Hu et al. (2000) for protons with (Case A) and without (Case B) the dispersive effect of the minor ions, respectively. Dotted and dashed lines indicate the $v_{1/e}$ profiles obtained by Hu et al. (2000) for O VI ions with (Case A) and without (Case B) the dispersive effect of the minor ions, respectively. On the right axis is shown the effective temperatures obtained through Eq. 3.

REFERENCES

- Allen, L. A., Habbal, S. R., & Hu, Y. Q. 1998, *J. Geophys. res.*, 103, 6551
- Antonucci, E. 1999, in *Eight SOHO Workshop: Plasma Dynamics and Diagnostics in the Solar transition Region and Corona*, eds. J.-C. Vial & B. Kaldeich-Schürmann, (Noordwijk: ESA), SP 446, 53
- Antonucci, E., Dodero, M. A., & Giordano, S. 2000, *Sol. Phys.*, 197, 115
- Arnaud, M., & Rothenflug, R. 1985, *A&AS*, 60, 425
- Banerjee, D., Teriaca, L., Doyle, J. G., & Wilhelm, K., 1998, *A&A*, 339, 208
- Banerjee, D., Teriaca, L., Doyle, J. G., & Lemaire, P. 2000, *Solar Phys.*, 194, 43
- Beckers, J. M., & Chipman, E. 1974, *Sol. Phys.*, 34, 151
- Brueckner, G. E., et al. 1995, *Sol. Phys.*, 162, 357

- Casalbuoni, S., Del Zanna, L., Habbal, S. R., & Velli, M. 1999, JGR, 104, 9947
- Cranmer, S. R., Kohl, J. L., Noci, G., et al. 1999, ApJ, 511, 481
- David, C., Gabriel, A. H., Bely-Dubau, F., et al. 1998, A&A, 336, L90
- DeForest, C. E., & Gurman, J. B. 1998, ApJ, 501, L217
- DeForest, C. E., Hoeksema, J. T., Gurman, J. B., et al. 1997, Sol. Phys., 175, 393,
- DeForest, C. E., Plunkett, S. P., & Andrews, M. D. 2001, ApJ, 546, 569
- Delaboudinière, J.-P., et al. 1995, Sol. Phys., 162, 291
- Del Zanna, G., Bromage, B. J. I., & Mason, H. E., 2002, A&A, in press
- Del Zanna, L., Hood, A. W., & Longbottom, A. W. 1997, A&A, 318, 963
- Doschek G. A., Warren, H. P., Laming J. M., et al. 1997, ApJ, 482, L109
- Esser, R., & Edgar, R. J. 2000, ApJ, 532, L71
- Fisher, R., & Guhathakurta, M. 1995, ApJ, 447, L139
- Gabriel, A. H. 1971, Sol. Phys., 21, 392
- Gardner, L. D., Kohl, J. L., Daigneau, P. S., et al. 1996, SPIE, 2831, 2
- Giordano, S., Antonucci, E., Benna, C., et al. 1997, in Fifth SOHO Workshop: The Corona and Solar Wind Near Minimum Activity, ed. A. Wilson, (Noordwijk: ESA), SP 404, 413
- Giordano, S., Antonucci, E., Noci, G., Romoli, M., & Kohl, J. L. 2000, ApJ, 531, L79
- Habbal, S. R., Esser, R., Guhathakurta, M., Sittler, E. C., & Fisher, R. R., 1995. Geophys. Res. Letters, 22(12), 1465
- Harrison, R. A., Sawyer, E. C., Carter, M. K., et al. 1995, Sol. Phys. 162, 233
- Hassler, D. M., Dammasch, I. E., Lemaire, P., et al. 1999, Science, 283, 810
- Hassler, D. M., Wilhelm, K., Lemaire, P., & Schühle, U., 1997, Sol. Phys., 175, 375
- Hu, Y. Q. Esser, R., & Habbal, S. R. 2000, JGR, 105, 5093
- Ko, Y. K., et al. 1997, Sol. Phys., 171, 345

- Kohl, J. L., Esser R., Gardner L. D., et al. 1995, *Sol. Phys.*, 162, 313
- Kohl, J. L., Noci, G., Antonucci, E., et al. 1997, *Sol. Phys.*, 175, 613
- Kohl, J. L., Noci, G., Antonucci, E., et al. 1998, *ApJ*, 501, L127
- Kohl, J. L., & Withbroe, G. L. 1982, *ApJ*, 256, 263
- Kopp, R. A., & Holtzer, T. E. 1976, *Sol. Phys.*, 49, 43
- Koutchmy, S. 1977, *Solar Phys.* 51, 399
- Krieger, A. S., Timothy, A. F., & Roelof, E. C. 1973, *Sol. Phys.*, 29, 505
- Lamy, P., et al. 1997, in *Fifth SOHO Workshop: The Corona and Solar Wind Near Minimum Activity*, ed. A. Wilson, (Noordwijk: ESA), SP 404, 491
- Lemaire, P., Wilhelm, K., Curdt, W., et al. 1997, *Sol. Phys.*, 170, 105
- Li, X., Habbal, S. R., Kohl, J. L., & Noci, G. 1998, *ApJ*, 501, L133
- Mariska, J. T. 1992, *The Solar Transition Region*, Cambridge University Press, Cambridge
- Mazzotta, P., Mazzitelli, G., Colafrancesco, S., & Vittorio, N., 1998, *A&AS*, 133, 403
- Noci, G., Kohl, J.L., & Withbroe, G. L. 1987, *ApJ*, 315, 706
- Noci, G., & Maccari, L. 1999, *A&A*, 341, 275
- Ofman, L., Nakariakov, V. M., & DeForest, C. E. 1999, *ApJ*, 514, 441
- Olsen, E. L., Leer, E., & Holzer, T. E., 1994, *ApJ*, 420, 913
- Patsourakos, S., & Vial, J.-C. 2000, *A&A*, 359, L1
- Raymond, J. C., Kohl, J. L., Noci, G., et al. 1997, *Sol. Phys.*, 175, 645
- Raymond, J. C., Mazur, J. E., Allegrini, F., et al. 2001, in *Solar and Galactic Composition*, ed. R. Wimmer-Schweingruber (New York:AIP), 49
- Rottman, G. J., Woods, T. N. & Sparn, T. P., 1993, *J. Geophys. Res.*, 98, 10667
- Tu, C.-Y., & Marsch, E. 1999, in *Solar Wind IX*, eds. S. R. Habbal, R. Esser, J. V. Hollweg & P. A. Isenberg (AIP Conference proc. 471), 373
- van de Hulst, H. C. 1950, *Bull. Astron. Inst. Neth.*, 11, 410, 135

- von Steiger, R., Vial, J.-C., Bochsler, P., et al. 2001, in *Solar and Galactic Composition*, ed. R. Wimmer-Schweingruber (New York:AIP), 13
- Walker, A.B.C., DeForest, C.E., Hoover, R.B., Barbee, T.D.W. 1993, *Solar Phys.*, 148, 239
- Wang, Y.-M. 1994, *ApJ*, 435, L153
- Widing, K. G., & Feldman, U. 1992, *ApJ*, 392, 715
- Wilhelm, K., Curdt, W., Marsch, E., et al. 1995, *Sol. Phys.*, 162, 189
- Wilhelm, K., Dammasch, I. E., Marsch, E., & Hassler, D. M. 2000, *A&A*, 353, 749
- Wilhelm, K., Lemaire, P., Curdt, W., et al. 1997, *Sol. Phys.*, 170, 75
- Wilhelm, K., Lemaire, P., Dammasch, I. E., Hollandt, J., Schühle, U., Curdt, W., Kucera, T., Hassler, D. M., & Huber, M. C. E. 1998, *A&A*, 334, 685
- Wilhelm, K., Marsch, E., Dwivedi, B., Hassler, D. M., Lemaire, P., Gabriel, A. H., & Huber, M. C. E. 1998a, *ApJ*, 500, 1023
- Wimmer-Schweingruber R., von Steiger, R., Geiss, J., et al. 1998, in *Solar Composition and its Evolution - From Core to Corona*, eds. C. Frohlich, M. C. E. Huber, S. K. Solanki & R. von Steiger (Dordrecht: Kluwer), 387
- Withbroe, G. L., Kohl, J. L., Weiser, H. & Munro, R. H. 1982, *Space Sci. Rev.*, 33, 17
- Zangrilli, L., Poletto, G., Nicolosi, P., Noci, G., & Romoli, M. 2002, *ApJ*, 574, 477